Atmospheric
Chemistry
and Physics

Diagnosing ozone–NO$_x$–VOC–aerosol sensitivity and uncovering causes of urban–nonurban discrepancies in Shandong, China, using transformer-based estimations

Chenliang Tao[1], Yanbo Peng[1,2], Qingzhu Zhang[1], Yuqiang Zhang[1], Bing Gong[3], Qiao Wang[1], and Wenxing Wang[1]

[1]Big Data Research Center for Ecology and Environment, Environmental Research Institute,
Shandong University, Qingdao 266237, PR China
[2]Shandong Academy for Environmental Planning, Jinan 250101, PR China
[3]Jülich Supercomputing Centre, Forschungszentrum Jülich, 52425 Jülich, Germany

Correspondence: Yanbo Peng (pengyanbo@mail.sdu.edu.cn) and Qingzhu Zhang (zqz@sdu.edu.cn)

Abstract. Narrowing surface ozone disparities between urban and nonurban areas escalate health risks in densely populated urban zones. A comprehensive understanding of the impact of ozone photochemistry on this transition remains constrained by current knowledge of aerosol effects and the availability of surface monitoring. Here we reconstructed spatiotemporal gapless air quality concentrations using a novel transformer deep learning (DL) framework capable of perceiving spatiotemporal dynamics to analyze ozone urban–nonurban differences. Subsequently, the photochemical effect on these discrepancies was analyzed by elucidating shifts in ozone regimes inferred from an interpretable machine learning method. The evaluations of the model exhibited an average out-of-sample cross-validation coefficient of determination of 0.96, 0.92, and 0.95 for ozone, nitrogen dioxide, and fine particulate matter (PM$_{2.5}$), respectively. The ozone sensitivity in nonurban areas, dominated by a nitrogen-oxide-limited (NO$_x$-limited) regime, was observed to shift towards increased sensitivity to volatile organic compounds (VOCs) when extended to urban areas. A third "aerosol-inhibited" regime was identified in the Jiaodong Peninsula, where the uptake of hydroperoxyl radicals onto aerosols suppressed ozone production under low NO$_x$ levels during summertime. The reduction of PM$_{2.5}$ could increase the sensitivity of ozone to VOCs, necessitating more stringent VOC emission abatement for urban ozone mitigation. In 2020, urban ozone levels in Shandong surpassed those in nonurban areas, primarily due to a more pronounced decrease in the latter resulting from stronger aerosol suppression effects and less reduction in PM$_{2.5}$. This case study demonstrates the critical need for advanced spatially resolved models and interpretable analysis in tackling ozone pollution challenges.

1 Introduction

Surface ozone (O$_3$), fine particulate matter (PM$_{2.5}$), and nitrogen dioxide (NO$_2$) are among the most important trace gases in the atmosphere that significantly impact the ecological environment and public health (Han and Naeher, 2006; Yue et al., 2017). During the Action Plan on the Prevention and Control of Air Pollution (denoted as the Clean Air Action, 2013–2017) (Action Plan on Air Pollution Preven-

tion and Control (in Chinese), 2023), PM$_{2.5}$ and nitrogen oxide (NO$_x$ = nitric oxide (NO) + NO$_2$) emissions across China decreased by 33 % and 21 %, respectively (Zheng et al., 2018), while surface O$_3$ exhibited an increasing trend (Lu et al., 2018). The increase in O$_3$ could be partially attributed to the "aerosol-inhibited" effect, where the reduction in PM$_{2.5}$ results in a diminished reactive uptake of hydroperoxyl radicals (HO$_2$) onto aerosols (Ivatt et al., 2022; Li et al., 2019). The societal benefits of reducing premature deaths

and economic losses from PM$_{2.5}$ reductions have been diminished by the rising O$_3$ (Liu et al., 2022). Thus, achieving the joint attainment objectives for PM$_{2.5}$ and O$_3$ has been set as the top priority for China's long-term air pollution control policies.

The complexity of O$_3$ formation is partly reflected by the nonlinear response to changes in precursors (i.e., volatile organic compounds – VOCs; NO$_x$), as well as the presence of heterogeneous reactions in aerosols. Understanding these dynamics is crucial to investigating currently narrowing differences in O$_3$ concentrations between urban and nonurban areas, which have traditionally shown higher levels in rural areas (Han et al., 2023). The formaldehyde-to-NO$_2$ ratio (HCHO / NO$_2$ or FNR) serves as a theoretical gauge of the relative abundance of total organic reactivity to hydroxyl radicals (OH) and NO$_x$ (W. Wei et al., 2022; Sillman, 1995), and as such, it can function as a useful indicator of O$_3$ sensitivity. Previous studies have utilized HCHO/NO$_2$ from satellite remote sensing to infer O$_3$ production regimes for guiding O$_3$ control policies (Jin et al., 2023, 2020; D. Li et al., 2021). However, the changes in the HCHO/NO$_2$ threshold in O$_3$ regime classification modulated by meteorology and localized atmospheric chemistry in space and time, as well as uncertainties relating columns to the surface, preclude robust applications over larger spatial scales (Lee et al., 2023; Jin et al., 2017; Souri et al., 2023). While the observation-based model method alleviates some of these limitations, constraints remain including computational demands and prior chemical mechanisms (K. Song et al., 2022; Chu et al., 2023). The advent of interpretable machine learning models affords new opportunities to unravel intricate dependencies governing O$_3$ formation purely from actual observational data. However, sparse ground-based monitoring stations, especially in rural areas, pose great challenges to the full spatial coverage of studies. Thus, the high-spatiotemporal-resolution estimations of surface air pollutants are urgently needed to improve our understanding of how these pollutants are changing and interacting.

Recent studies have utilized spatially resolved remote sensing data to estimate the continuous distribution of air pollutants in space by diverse machine learning (ML) models (Lyapustin and Wang, 2022; Lamsal et al., 2022; Huang et al., 2021; Li and Wu, 2021; X. Ren et al., 2022), such as random forest (RF), full residual deep learning, and Bayesian ensemble modeling. These attempts have demonstrated the tremendous potential of machine learning as an alternative to atmospheric chemical models (Jung et al., 2022). Nevertheless, there are still several aspects that have not been fully considered. For instance, coarse-resolution maps limit the ability to characterize the fine-scale variation of air pollution within urban areas, which has significant implications for environmental justice disparities of disadvantaged communities (Jerrett et al., 2005; X. Ren et al., 2022; Dias and Tchepel, 2018). Additionally, existing ML models may not fully account for the complex atmospheric chemistry and physics processes that influence pollutant concentrations due to the single-pixel-based processing mode (Huang et al., 2021; Requia et al., 2020; Thongthammachart et al., 2022; M. Li et al., 2022; Geng et al., 2021). Although several efforts have been made using a neural network with convolutional layers (Di et al., 2016) and explicitly incorporating spatiotemporally weighted information into machine learning models (Wei et al., 2022b), the global spatiotemporal self-correlation of multidimensional features in the input array has remained unaddressed. Meanwhile, convolutional operations extract features from all neighboring grids of the target, ignoring the fact that the environmental knowledge of the target grid itself is the most significant, with the adjacent features being secondary.

In this study, we aim to analyze the evolving dynamics of urban–nonurban O$_3$ differences between 2019 and 2020. The roles of emission discrepancies and nonlinearity of O$_3$–NO$_x$–VOC–aerosol photochemical processes in shaping these O$_3$ variations were deeply dissected. To achieve a comprehensive analysis, we employed a new spatiotemporal transformer framework that paid special attention to air mass transport and dispersion affected by spatial–temporal correlations to reconstruct spatially gapless air quality datasets based on satellite data, ground-level observations, and meteorological reanalysis. The estimations are particularly vital for regions lacking dense ground-based monitors, ensuring that our understanding of O$_3$ dynamics in urban–nonurban areas and formation regimes is not limited by geographical constraints in data availability. Surface O$_3$ formation regimes in Shandong province were inferred by the classic XGBoost model (Chen and Guestrin, 2016) coupled with Shapley Additive exPlanations (SHAP) (Lundberg and Lee, 2017), which identifies the impact of meteorological conditions and photochemical indicators (i.e., PM$_{2.5}$ as a proxy for aerosols, NO$_2$ as a proxy for NO$_x$, and HCHO as a proxy for VOCs) on O$_3$. The innovative transformer-based modeling and interpretable machine learning analysis approaches are expected to enable new applications such as those of air quality simulation and O$_3$ formation regime studies.

2 Materials and methods

2.1 Predictor variables

The study domain covered the Shandong province of China, which has a high mortality burden of air pollution (Liu et al., 2017). The surface PM$_{2.5}$, O$_3$, and NO$_2$ concentration measurements were collected from the regulatory air quality stations of the China National Environmental Monitoring Center (CNEMC, with a total of 179 locations) and the Shandong Provincial Eco-environmental Monitoring Center (SDEM, with a total of 166 locations) (Fig. S1 in the Supplement). The SDEM stations were included to fill the spatial gaps in the county and rural areas where CNEMC stations were lacking. The study area was divided into 1.22 million

grid cells with a spatial resolution of 500 m. We utilized a range of predictor data, including tropospheric NO$_2$ vertical column densities (VCDs) and O$_3$ total VCDs measured by the TROPOspheric Monitoring Instrument (TROPOMI) (Lamsal et al., 2022; Copernicus Sentinel-5P (processed by ESA), 2020), aerosol optical depth (AOD) data and atmospheric properties obtained from the Moderate Resolution Imaging Spectroradiometer (MODIS) Multi-Angle Implementation of Atmospheric Correction products (Lyapustin and Wang, 2022), AOD estimates from Modern-Era Retrospective Analysis for Research and Applications as the supplement to MODIS (Global Modeling and Assimilation Office (GMAO), 2015), meteorological reanalysis obtained from the fifth-generation atmospheric reanalysis dataset of the European Centre for Medium-Range Weather Forecasts (ECMWF) (ERA5) (Hersbach et al., 2023, p. 5), daily dynamic industrial emissions, moonlight-adjusted nighttime light products (Román et al., 2018), vegetation index (Didan, 2021), population density (WorldPop, 2018), road density, land use data (Jun et al., 2014), and the Shuttle Radar Topography Mission digital elevation model. The detailed information for all predictive variables is listed in Table S1 and discussed in Sects. S1–S2. Taking space-variant and seasonal patterns into consideration, several spatiotemporal indicators such as geographical coordinates, Euclidean spherical coordinates, year, Julian date, and helix-shaped trigonometric sequences were also included as predictor variables (Sect. S3) (Sun et al., 2022). Geographic information system techniques, including reprojection and resampling, were used to consolidate all the data obtained for consistent projection and spatial scale. Finally, the Light Gradient Boosting Machine was used to fill satellite data gaps (Sect. S4) (Ke et al., 2017).

2.2 Air Transformer

AiT is an individual transformer model that adopts an encoder–decoder architecture with multidimensional self-attention computation to dynamically capture the spatiotemporal autocorrelation of atmospheric pollution changes from the sequences of pixels and variables for more reliable spatial maps of estimation. Compared with existing image and video recognition transformers, such as ViT (Dosovitskiy et al., 2021), Timesformer (Bertasius et al., 2021), and Uniformer (K. Li et al., 2021), AiT is innovative in incorporating self-attention across channels after the pixel-based self-attention and taking advantage of the decoder. The former can capture the correlations between predictor variables. The decoder was employed to enable interaction between the primary target grid and neighboring grids. Predictor variables with eight time steps within 1000 m of the target grid cell were fed into the model to learn spatiotemporally disparities among atmospheric pollutants for predicting O$_3$, NO$_2$, and PM$_{2.5}$ within the target grid point.

The overall architecture of the proposed AiT model and the dimensions of input data are illustrated in Fig. 1. The encoder maps an input sequence with neighborhood spatiotemporal data to a sequence with high-dimensional spatiotemporal characteristics, and the decoder generates an estimation by computing self-attention representations between the target grid and outputs of the encoder. The encoder of AiT takes as input a clip $X \in R^{V \times T \times H \times W}$ consisting of T multivariable frames of size $H \times W$ sampled from the original dataset, where V is the number of variables and the target grid cell is located at $(\lceil \frac{H}{2} \rceil, \lceil \frac{W}{2} \rceil)$. The decoder takes as input a clip $X \in R^{V \times 1 \times 1 \times T}$ consisting of V variables from the target grid. Several transformer blocks with modified self-attention computation (AiT blocks) are applied to the encoder. The AiT encoder block is similar to the standard vision transformer block but specifically designed for atmospheric estimation (Dosovitskiy et al., 2021). It is a stack of two self-attention schemes, including global spatiotemporal self-attention on the pixels and channel self-attention on variable predictors. The former contains $N = HW$ effective input sequence length for the self-attention to extract spatiotemporal information. The latter computes self-attention based on V effective input sequence length to capture hidden information on variables. The decoder part is symmetric to the encoder part, but it only has a block with the spatiotemporal self-attention mechanism. We compute the matrix of self-attention outputs as

$$\text{Attention}\,(Q, K, V) = \text{softmax}\left(\frac{QK^T}{\sqrt{d_k}} + B\right)V, \tag{1}$$

where Q, K, and V are the queries, keys, and values in the inputs of the particular attention, respectively. d_k is the feature dimensionality of K, and B is the geographic positional bias term. Another difference is that the attention function of the decoder is computed on Q from the estimated grid data and (K, V) from the outputs of encoder blocks under the same stage, resulting in the outputs of the last decoder block being sized 1×128. The description of the data transformation and design details in the process of training can be found in Sect. S5 in the Supplement. The multi-task learning strategy was also applied for learning representation across multiple pollutant estimation tasks (Sect. S6). The aggregated feature data from June 2019 to June 2021 were utilized to train and validate the model through cross-validation (CV), where the optimal model, trained based on out-of-sample CV, was used to estimate multiple pollutant concentrations during the study period, which was then employed for subsequent analysis.

2.3 Diagnosing O$_3$ formation sensitivity

Interpretability can provide insight into how a model may be improved, bolster the understanding of the process being modeled, and engender appropriate confidence among researchers. SHAP is a coalitional game-theoretic approach based on Shapley values (Shapley, 1988) that assigns each
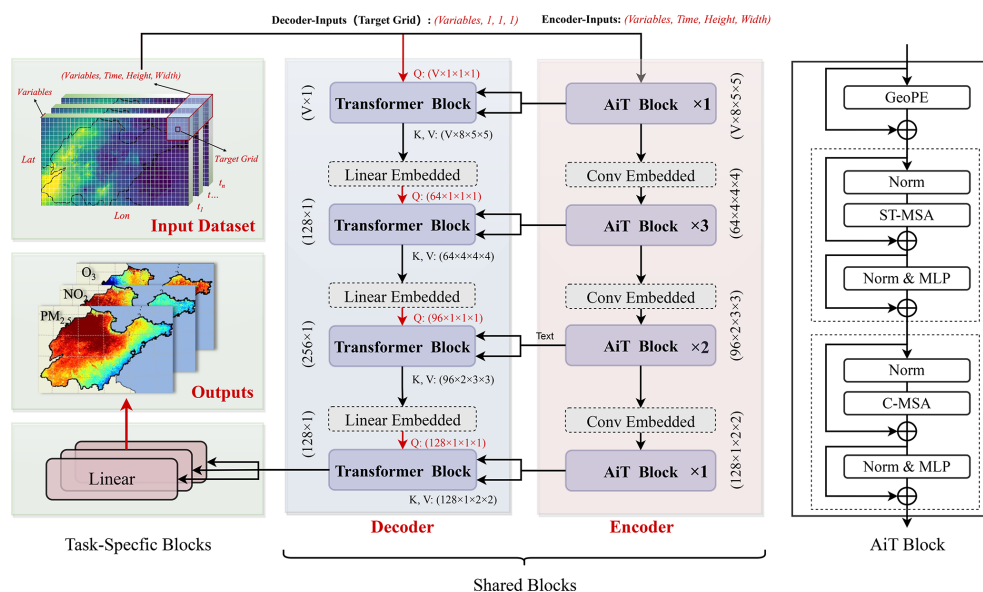
Figure 1. Schematic diagram of the AiT model. The white box of multi-dimension inputs presents each pixel of raster data. The AiT block is a transformer block based on self-attention across space, time, and variables. GeoPE, Norm, MLP, ST-MSA, and C-MSA respectively indicate positional embedding, layer normalization, multi-layer perceptron, spatial–temporal multi-head self-attention, and multi-channel (multi-variables) multi-head self-attention.

variable an importance value for a particular estimation. Deep SHAP, a high-speed approximation algorithm that builds on the connection between Shapley values and DeepLIFT (Shrikumar et al., 2019), is employed to compute the feature importance of AiT from all data with monitoring labels for interpreting the prediction. The sensitivity of the O$_3$ formation regime was deduced using a combination of the XGBoost model and SHAP interpretability method, employing the GPUTreeShap algorithm (Mitchell et al., 2020), which simulated the response of surface O$_3$ to meteorological conditions, HCHO, NO$_2$, and PM$_{2.5}$, by utilizing the continuous estimations from ERA5, AiT, and TROPOMI between 2019 and 2020. The incorporation of meteorology in the model ameliorated the inadequacies in the conventional method (HCHO to NO$_2$ ratio), where its thresholds for identifying O$_3$ regimes vary temporally and spatially. The positive or negative contributions of three atmospheric pollutants were used to identify their promoting or inhibitory effects on O$_3$ variability. Given the unbiased property of SHAP values regarding directionality, the normalized relative magnitudes of SHAP values were calculated for HCHO, NO$_2$, and PM$_{2.5}$. This allowed the differentiation of the O$_3$ formation regimes based on the locally maximal proportions of the SHAP values for each species. The ground-level monthly HCHO concentrations were derived using a combination of the column-to-surface conversion factor (CF) simulated from the ECMWF Atmospheric Composition Reanalysis 4 and the tropospheric HCHO VCDs obtained from TROPOMI (Cooper et al., 2022; Su et al., 2022; Inness et al., 2019). A detailed description of the CF method as used here is dis-

cussed in Sect. S7. To ensure consistency in resolution between TROPOMI and AiT, we employed the oversampling method to downscale the TROPOMI VCDs to the resolution of AiT estimation, which has been proven effective in achieving finer resolution (Su et al., 2022; Cooper et al., 2022; van Donkelaar et al., 2015).

3 Results and discussion

3.1 Performance evaluation for the AiT

3.1.1 Cross-validation metrics

We evaluated the AiT performance using the 10-fold CV approach (Sect. S8), with the correlation coefficient (R^2) measuring the extent to which model simulations explain variability in atmospheric pollutants and root mean square error (RMSE) and mean absolute error (MAE) evaluating the bias and error of the estimates. As shown in Fig. 2, out-of-sample CV daily ground-level O$_3$, NO$_2$, and PM$_{2.5}$ estimations are highly consistent with ground observations ($R^2 = 0.96, 0.92, 0.95$), indicating low uncertainties, with RMSE of 10.1, 4.7, and 8.5 µg m^{-3} and MAE of 7.2, 3.5, and 5.3 µg m^{-3} for the 2018–2021 period. The linear regression comparing the O$_3$ predictions versus observations yields a slope of 0.98 and an intercept of 2.39, which demonstrates that there is no systematic bias in the estimations. Meanwhile, as shown in Fig. S3, our AiT model performs well at the individual site scale with high CV RMSE for O$_3$, NO$_2$, and PM$_{2.5}$ (10.5 ± 8.6, 4.7 ± 1.1, and 8.3 ± 2.8 µg m^{-3}). In general, the AiT model is robust for multi-pollutant simultaneous estimations.
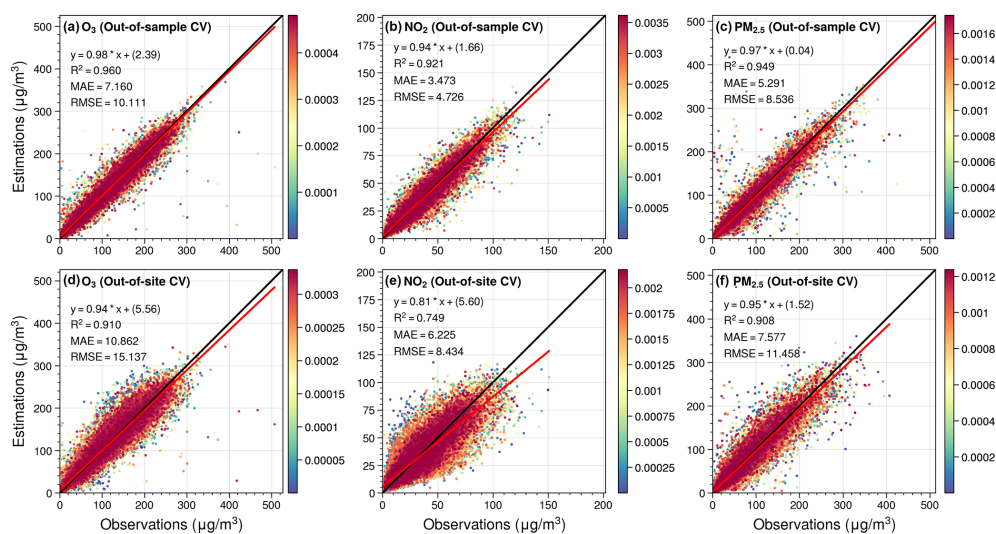
Figure 2. Out-of-sample cross-validation (**a–c**) and out-of-site cross-validation (**d–f**) of daily ground-level O$_3$, NO$_2$, and PM$_{2.5}$ concentration in the validation set.
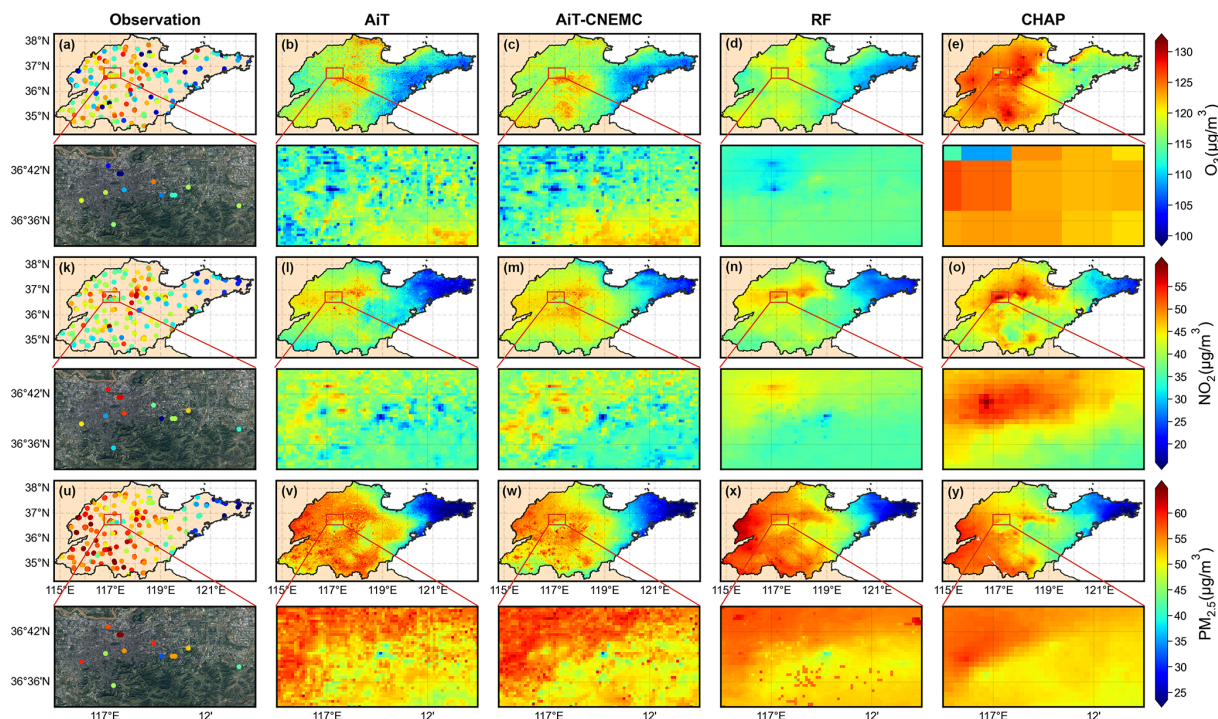

Figure 3. Spatial distribution of the annual mean (**a–e**) O$_3$, (**k–o**) NO$_2$, and (**u–y**) PM$_{2.5}$ concentrations from observations, Air Transformer (AiT), CNEMC-trained AiT, random forest (RF), and ChinaHighAirPollutants (CHAP), respectively, in 2019. The region enclosed by the red rectangular box corresponds to the zoomed-in maps of the satellite (©Tianditu: https://www.tianditu.gov.cn/, last access: 23 January 2024) and pollutant concentrations at a city scale for the capital city of Shandong province, Jinan.

The spatial generalization ability of the AiT is then examined by the out-of-site CV evaluation method (Fig. 2). The daily spatial variations of O$_3$, NO$_2$, and PM$_{2.5}$ at locations without ground measurements can be well estimated by our model (i.e., CV $R^2 = 0.91$, 0.75, 0.91), representing a core contribution of such studies. We also probe the model per-

formance for each site separately based on spatial CV estimations (Fig. S4). This general model yields an RMSE of 15.2 ± 8.8, 8.1 ± 2.7, and 11.1 ± 2.8 µg m^{-3}, respectively. Furthermore, we trained the AiT model using data exclusively from CNEMC and assessed its generalizability by validating it with data from SDEM. The model demonstrates strong

performance with high our-of-sample CV R^2 values in the validation dataset of CNEMC (Fig. S5), and when evaluated with SDEM data, it exhibits only an acceptable degradation in predictive accuracy (Fig. S6, R^2 for O_3, NO_2, and $PM_{2.5}$: 0.90, 0.73, 0.79). Meanwhile, our framework utilizes multi-task learning to enhance computational efficiency through a single iteration and leverages the interactions among multiple pollutants to optimize the performance at individual pollutant levels (Table S2). In summary, AiT provides relatively stable estimations in areas without available ground-level monitoring and reliably extends ground monitoring from the site scale to the full-coverage spatial scale with high spatial resolution.

3.1.2   Compared with other ML models

Since ground-level air quality measurements across the target regions are extremely limited at a 500 m spatial resolution, representing only roughly 2 / 1000 of the total grid cells, we seek implicit approaches to validate our estimated near-surface pollutant concentrations. We compared the model performance with previous studies that applied different ML methods to estimate these three air pollutants individually and found that our cross-validation results are comparable to or even better than those (Table S3). We also created a new dataset in our study by applying the classic RF algorithm, which is the most common ML model for estimating atmospheric pollution in recent years (Wei et al., 2022a; Requia et al., 2020; Xiao et al., 2018; Geng et al., 2021; Lu et al., 2021) with the same variables as AiT. The statistical comparisons between AiT and RF are also shown in Table S3. We then compared the spatial distribution of our results with estimations from CHAP, AiT-CNEMC, and RF.

Figure 3 shows the spatial maps of near-surface air pollutants with partially zoomed satellite images for monitoring sites, AiT, CNEMC-trained AiT, RF, and CHAP in 2019 (see Fig. S7 for 2020). We found that the estimated NO_2 and $PM_{2.5}$ from the AiT share a similar spatial distribution to those estimated by RF and CHAP. However, enlarged city-level urban regions in Fig. 3 reveal that AiT estimates fine structures and intra-urban disparities in near-surface multi-pollutant concentrations, which cannot be captured by either RF or CHAP products. This spatial gradient is also captured by AiT trained with CNEMC data, revealing the reliability of the deep learning model structure. In general, while RF and CHAP can only identify the hotspots of air pollutants at a regional scale, the spatial distribution of air pollutants estimated by AiT shows much more detailed differences with high spatial and temporal variability across the city scale. The differences of near-surface annual averaged pollutants between 2019 and 2020 for measured and multi-estimated data are presented in Fig. S8. The reductions or increases in O_3, NO_2, and $PM_{2.5}$ in distinct locations can be simulated by our model, which is relatively consistent with the changes in measurements. The zoomed maps in Fig. S8 show the differ-

ences in three pollutant concentrations at the city scale of the capital of Shandong province, Jinan. It can be found that the change in pollutant levels in 2020 compared to 2019 exhibits substantial regional variations and intra-urban heterogeneity, with some areas experiencing an increase and others a decrease. Compared to the estimations of RF and CHAP, our results successfully capture the complex distribution of air pollution in reality and reveal that the decline in $PM_{2.5}$ is primarily concentrated in suburban areas, while an increase is pronounced in some urban regions during 2020. Notably, this spatial trend may be consistent with underlying emission patterns and meteorological conditions.

3.1.3   Typical event study

The typical example of the spatial distribution of multi-pollutant observations and estimations of AiT is compared for validating the predictive capability of the model during a particular pollution episode, i.e., 13–16 March 2021. During this period, an early-season dust storm, which was called the largest and strongest such storm in a decade, hit northern China (Myers, 2021). As shown in Fig. 4, our model can capture the spatial distribution of surface O_3, NO_2, and $PM_{2.5}$ at the time of severe atmospheric pollution. In addition, our estimations are in high concordance with measurements in terms of magnitudes and spatial variability over the entire research region. The model trained solely on CNEMC data is also capable of effectively capturing the drastic changes in air quality during the pollution episode (Fig. S9). Combining wind fields to analyze $PM_{2.5}$ distribution on the day of the dust storm, it can be found that surface wind carries a massive amount of particulate matter from Beijing, which suffered a severe dust storm, to northern Shandong. The influence was gradually diminishing in southern Shandong due to the obstruction of Mount Tai. Spatial heterogeneity within intra-urban areas was further investigated to identify the hotspots of pollution sources. The satellite images in even-numbered rows of Fig. 4 illustrate the spatial disparities of three pollutants around four typical emission sources: thermal power plants, industrial parks, overpasses, and parks. As depicted, these anthropogenic emission sources contribute to higher pollution levels, while the mountain in the park mitigates primary pollution but also increases O_3 concentrations. Industrial sources emit a large amount of NO_x and $PM_{2.5}$, leading to increased pollution of these species compared with other urban microenvironments, which in turn promotes O_3 formation, particularly in downwind areas (Miller et al., 1978; Tang et al., 2020). Although the spatial gradients of pollutants on the street are not as apparent as in the dataset with 100 m resolution (Huang et al., 2021), the predicted spatial variation between various geographical scenes is in satisfactory agreement given the 500 m scale of the model. Urban areas affected by diverse dust pollution exhibit lower $PM_{2.5}$ concentrations compared to rural areas due to the obstructive and filtering effects of artificial structures, such as buildings
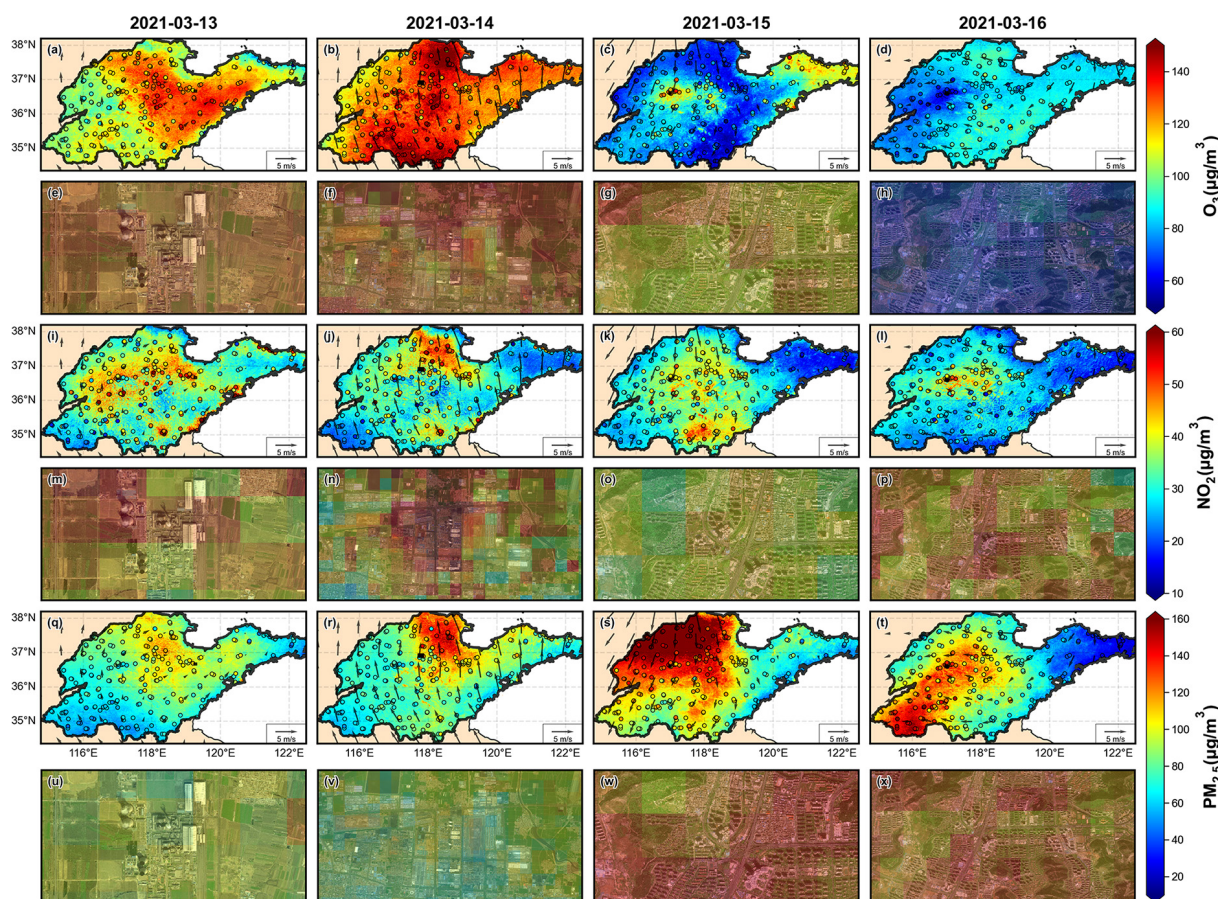
Figure 4. The spatial distribution of ground-level O$_3$ **(a–d)**, NO$_2$ **(i–l)**, and PM$_{2.5}$ **(q–t)** concentrations from AiT and monitoring stations during 13–16 March 2021 in Shandong, China. The black arrows are the 10 m wind speed and wind direction. The even-numbered rows correspond to the concentration distribution maps of typical emission sources for the respective pollutants, accompanied by satellite images (©Tianditu: https://www.tianditu.gov.cn/, last access: 23 January 2024). The upper right area of **(e)**, **(m)**, and **(u)** is a thermal power plant in Weifang (119°250′–119°280′E, 36°658′–36°673′N). The center area of **(f)**, **(n)**, and **(v)** is an industrial park in Zibo (117°725′–117°845′E, 36° 880′–36°940′N). The center and upper right area of **(g)**, **(o)**, and **(w)** represent an overpass and Wanling Mountain in Jinan (116°977′–117°009′E, 36°590′–36°606′N). The center area of **(h)**, **(p)**, and **(x)** is another overpass in Jinan (116°970′–117°030′E, 36°580′–36°610′N).

and urban greenery (Fig. S10), which cannot be effectively captured solely by ground-based observations. Notably, the elevated PM$_{2.5}$ inhibits the formation of O$_3$ by diminishing solar radiation flux and absorbing the HO$_2$ radical on the aerosol surface, even in conditions characterized by similar NO$_2$ levels. As for the mapping, AiT accurately grasps the spatial characteristics of air pollutants and delivers a coherent spatial–temporal distribution that is consistent with the prior knowledge of atmospheric transport.

3.2 Urban–nonurban difference

Full-coverage pollutant estimates provide a foundational basis for assessing urban–nonurban disparities, addressing the critical issue of imbalanced site numbers between urban and rural locations. Table S4 shows the concentrations of O$_3$, NO$_2$, PM$_{2.5}$, and HCHO over the urban and nonurban regions, delineated from an annual urban extent dataset (Zhao

et al., 2022). The urban extents in Shandong province in 2019 are depicted in Fig. S11. From 2019 to 2020, surface air pollutant levels declined significantly in Shandong. The averaged concentration discrepancies of these pollutants between urban and nonurban areas over February to March (lockdown during COVID-19) and June to October (summertime) are shown in Fig. 5. Surface concentrations of NO$_2$ and HCHO are higher in urban than nonurban areas, and the differences narrowed from February to October, while PM$_{2.5}$ is the opposite in both. Ground-level O$_3$ levels exhibited unexpected urban–nonurban disparity variations from the lockdown period through the summer as well as from 2019 to 2020. Compared to nonurban areas, the urban areas, which previously had lower O$_3$ levels, began to experience higher concentrations, attributed to a more rapid decline of ozone in nonurban regions. Figure 6 reveals that urban–nonurban differences in O$_3$ and PM$_{2.5}$ varied across various cities during the lock-
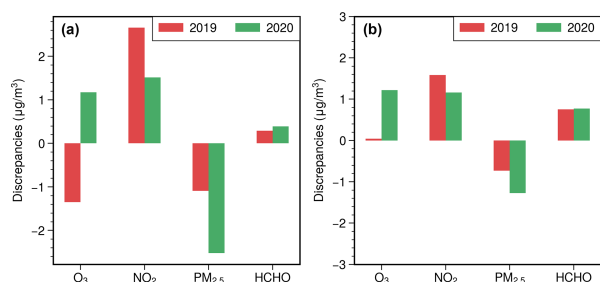
Figure 5. The discrepancies of O$_3$, NO$_2$, and PM$_{2.5}$ between urban and nonurban areas from 2019 to 2020 for the lockdown period **(a)** and the summertime **(b)** averaged concentration.

down period in 2019, while the higher NO$_2$ pollution in urban areas remained consistent. In summer, only a handful of urban areas exhibit lower levels of ozone concentration, where NO$_2$ and PM$_{2.5}$ levels surpass those in nonurban regions, attributable to a more pronounced titration effect of NO and a slower rate of photochemistry reactions (Fig. S12) (Sicard et al., 2016, 2020; Zhang et al., 2004). Comparative urban–nonurban differences from 2019 to 2020 indicate an accelerated reduction of ozone and HCHO in nonurban areas, while NO$_2$ and PM$_{2.5}$ levels in urban areas saw a more significant decrease due to the decline in anthropogenic activities, particularly the suspension of emissions from pollution sources located in urban areas. Upon comparing the results of urban–nonurban disparities of our data with monitoring data and the CHAP dataset, we have identified potential overestimations or underestimations across various cities in monitoring data, likely resulting from the limited number of nonurban sites (Figs. 6m and S13). The notable disparity between the number of urban and nonurban sites in cities such as JNA, LC, LY, QD, and YT results in a pattern of urban–nonurban differences that contrasts markedly with that observed in AiT (Table S5). The urban–nonurban difference calculated by CHAP generally aligns with our findings (Fig. S14). Nevertheless, it is worth noting that the coarse resolution of O$_3$ (10 km) has led to a significant overestimation. These results highlight the value of high-resolution and gapless data for studying urban–nonurban disparities.

3.3 Photochemical regimes

3.3.1 Ozone–NO$_x$–VOC–aerosol sensitivity

Figure S15 shows the seasonal maps of O$_3$, PM$_{2.5}$, and NO$_2$ estimations from AiT and satellite-derived surface HCHO. Based on these data, we first capture the well-established nonlinearities in O$_3$–VOC–NO$_x$ chemistry with a conceptual framework similar to classic O$_3$ isopleths typically generated with models (Pusede et al., 2015; J. Ren et al., 2022). Figure 7a depicts O$_3$ concentration as a function of HCHO and NO$_2$, which was derived solely from ground-level estimation. The result indicates that the O$_3$ regimes can be

qualitatively identified based on the nonlinear interaction between surface O$_3$, HCHO, and NO$_2$. In the regime characterized by high NO$_2$ and low HCHO, the elevated consumption of HO$_x$, predominantly driven by the OH + NO$_2$ termination reaction, results in the suppression of NO$_x$ on O$_3$, indicating the prevalence of VOC-limited chemistry. Conversely, when HCHO levels are high and NO$_2$ levels are relatively low, O$_3$ increases with NO$_2$ and exhibits insensitivity to HCHO due to abundant peroxyl radical (HO$_2$+ organic peroxy (RO$_2$) radicals, RO$_x$) self-reactions, suggesting NO$_x$-limited (VOC-saturated) chemistry. In cases where high HCHO and NO$_2$, the O$_3$ increases with both HCHO and NO$_2$, reaching a peak. While Fig. 7a resembles this overall O$_3$–VOC–NO$_x$ relationship, the blurry transition between two different regimes and the role of PM$_{2.5}$ are uncertain, which may be influenced by meteorological conditions, chemical and depositional loss of O$_3$, errors of estimations, and aerosol-inhibited regimes. Increasing PM$_{2.5}$ levels could suppress O$_3$ formation even under high HCHO and NO$_2$ conditions (Fig. 7b), which could be induced by enhanced reactive uptake of HO$_2$ onto aerosol particles and weaker photochemical reaction resulting from the scattering and absorption of solar radiation by anthropogenic aerosols. The relationship between PM$_{2.5}$ and O$_3$ in Shandong demonstrates the distinct stages of O$_3$ chemistry, as depicted in Fig. 7c. When PM$_{2.5}$ was below the maximum turning point (MTP1, 35 µg m^{-3}), a linear and positive correlation between O$_3$ and PM$_{2.5}$ was observed due to the common dependence on precursors in the initial stage (Zhang et al., 2022). As PM$_{2.5}$ increased beyond the MTP1, a sharp reduction in HCHO and O$_3$ was observed, accompanied by a decline in surface shortwave radiation, reflecting their formation as photooxidation products of OVOCs and NO$_x$. When PM$_{2.5}$ exceeded the minimum transition point (MTP2, 45 µg m^{-3}), a phase was observed with stagnant radiation intensity and relatively higher NO$_2$ levels compared to HCHO. This is typically associated with a VOC-limited regime, where an increase in HCHO and a decrease in NO$_2$ concentration could promote O$_3$ production. However, our findings demonstrated an opposite impact of HCHO and NO$_2$ on O$_3$ when PM$_{2.5}$ exceeded MTP2. Figure 7d shows the changes in the quantitative relationships between HCHO/NO$_2$ (FNR) and O$_3$ by artificially changing PM$_{2.5}$ and precursor levels for XGBoost, in which the peak of curves marks the transitional threshold of O$_3$ regimes from VOC- to NO$_x$-sensitive. It can be seen that attenuated PM$_{2.5}$ pollution could increase the sensitivity of O$_3$ to VOCs and decrease the sensitivity to NO$_x$, which causes the shift in O$_3$ regimes from NO$_x$-limited to VOC-limited. With the recent reduction in NO$_x$ emissions in China, the anticipated transition of the O$_3$ production regime in urban areas towards being more NO$_x$-limited has been impeded by the heightened VOC sensitivity resulting from decreased PM$_{2.5}$ levels. Our results are consistent with the findings of Li et al. regarding the O$_x$–NO$_x$ relationship in response to changing PM$_{2.5}$ (C. Li et al., 2022) and with

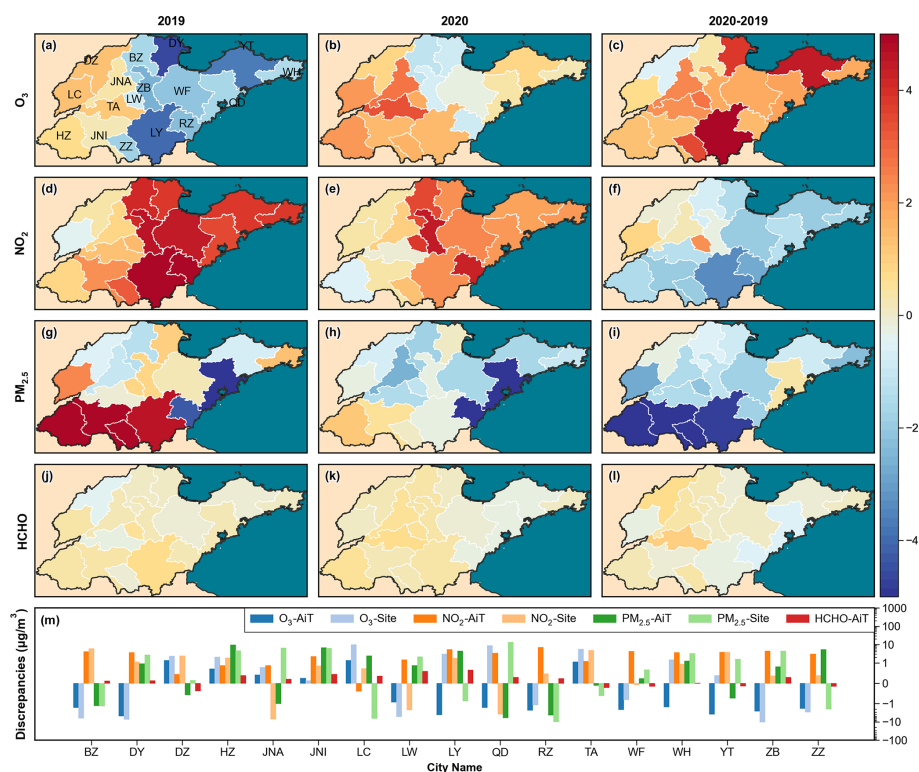**Figure 6.** The urban–nonurban disparities of O$_3$, NO$_2$, PM$_{2.5}$, and HCHO calculated by AiT across cities with administrative divisions in Shandong, China, during lockdown periods in 2019 **(a, d, g, j)** and 2020 **(b, e, h, k)**, as well as the changes in differences between 2019 and 2020 **(c, f, i, l)**. Panel **(m)** is the comparison between the results of monitoring station data and the AiT dataset in 2019. Red represents a greater decline in air pollutants in nonurban areas, while blue indicates a more significant reduction in urban areas in the third column of the figure (YT: Yantai, BZ: Binzhou, DY: Dongying, WH: Weihai, DZ: Dezhou, JNA: Jinan, QD: Qingdao, WF: Weifang, ZB: Zibo, LC: Liaocheng, LW: Laiwu, TA: Taian, LY: Linyi, RZ: Rizhao, JNI: Jining, HZ: Hezhe, ZZ: Zaozhuang).

the findings of Dyson et al. (2023) on the impact of HO$_2$ aerosol uptake on O$_3$ production (Dyson et al., 2023). The SHAP interaction plots in Fig. 7e and f illustrate that the influence of NO$_2$ and HCHO on O$_3$ formation is not constant and is influenced by the levels of PM$_{2.5}$. Typically, at a certain level of PM$_{2.5}$, a lower NO concentration results in a stronger inhibitory effect on O$_3$ production. This could be due to aerosols exerting stronger suppression through the HO$_2$ sink at lower NO$_x$ levels. As the concentration of PM$_{2.5}$ increases, often accompanied by a concurrent increase in NO$_2$ as a key precursor, there is a greater need for higher levels of NO$_2$ to be converted into nitrous acid (HONO) through the heterogeneous uptake by aerosols. This process produces more OH radicals, which facilitate photochemical O$_3$ formation, thereby offsetting the increased inhibitory effect of the HO$_2$ sink. Under high PM$_{2.5}$ concentrations, an increase in NO$_2$ along with a decrease in HCHO enhances their effect on promoting O$_3$ formation. Meanwhile, the impact of HCHO shifts from promoting to suppressing as PM$_{2.5}$ pollution intensifies. It further illustrates that the scavenging of HO$_2$ on aerosols can cause the shift in O$_3$ regimes from being VOC-limited to NO$_x$-limited and the threshold

approach is restricted by aerosols and meteorology for determining the constantly changing O$_3$ formation regimes over time and space.

Unraveling the intricate interplay of O$_3$ with meteorology, aerosols, and precursors that govern O$_3$ formation over extensive spatial domains has long confounded robust interpretation. These multiscale processes were elucidated using an interpretable ML model, which can quantify the positive or negative contributions of individual processes. As depicted in Fig. S16, the performance of the XGBoost model is robust, evidenced by a high R^2 value of 0.99 coupled with a low RMSE of 3.24 µg m^{-3} and MAE of 2.33 µg m^{-3}. Figure S17 shows that meteorological variations, chiefly surface shortwave radiation flux modulating photochemical reaction kinetics, primarily dictate the heterogeneous geographic distribution of O$_3$ at the regional scale, with lower levels over the Jiaodong Peninsula. Meanwhile, local atmospheric chemical processes predominate the city-scale variability of O$_3$. HCHO facilitated O$_3$ formation in urban areas yet suppressed it in rural regions across areas with high ozone, where most NO$_2$ promoted O$_3$ production overall, indicating VOC–NO$_x$ synergistic control on O$_3$ in cities and a NO$_x$-limited regime
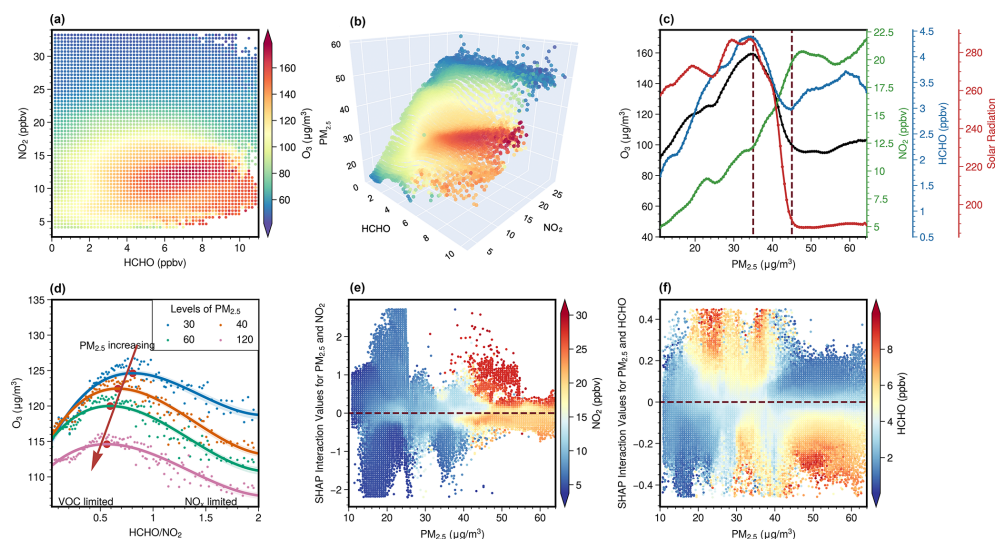
Figure 7. (a) O$_3$ concentrations as a function of surface HCHO and NO$_2$. **(b)** O$_3$ concentrations as a function of surface HCHO, NO$_2$, and PM$_{2.5}$. Both **(a)** and **(b)** utilize a shared color bar to indicate O$_3$ concentrations, enhancing comparability. **(c)** Relationship between O$_3$, and NO$_2$, HCHO, and surface shortwave radiation flux. The paired O$_3$, HCHO, NO$_2$, and solar radiation are divided into 100 bins based on PM$_{2.5}$, and then the averaged concentrations (*y* axis) are calculated for each PM$_{2.5}$ bin (*x* axis). **(d)** Changes in the HCHO/NO$_2$–O$_3$ relationship in response to changing PM$_{2.5}$ by the XGBoost model. The solid lines are fitted with fourth-order polynomial curves, and the shading indicates 95 % confidence intervals. **(e–f)** The interaction between SHAP values reveal an interesting hidden relationship between pairwise variables (PM$_{2.5}$, NO$_2$, HCHO) and O$_3$.
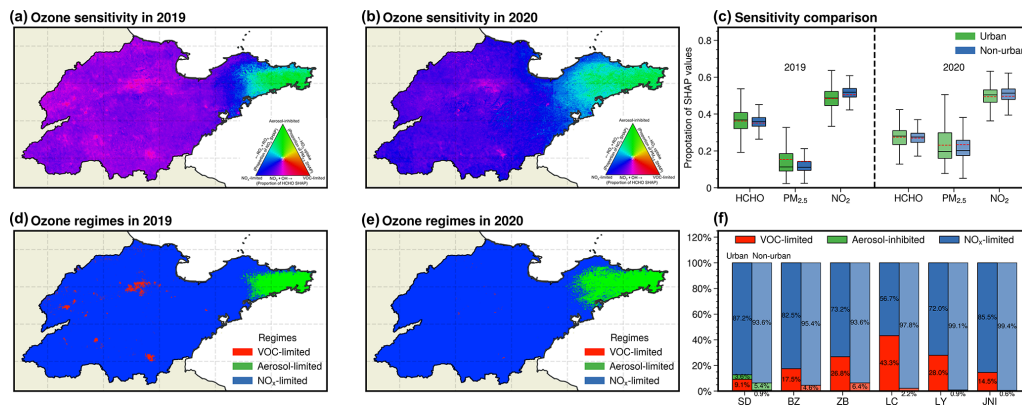

Figure 8. Comparison of geographical distribution for ozone formation regimes between 2019 and 2020 in the summertime. All surface daily O$_3$, PM$_{2.5}$, and NO$_2$ estimations from Air Transformer (AiT) are averaged over each month from May to October 2019–2020 for matching monthly HCHO derived from TROPOMI (500 · 500 m). **(a, b)** Geographical distribution of the fractional contribution of chemical factors representing O$_3$ formation regimes. The ternary phase diagram in the legend depicts the normalized fraction of SHAP values for O$_3$ attributed to HCHO, NO$_2$, and PM$_{2.5}$ at the surface, representing VOC-limited (red), aerosol-inhibited (green), and NO$_x$-limited (blue) regimes, respectively. **(c)** Statistical changes in the fractional contribution of chemical factors. **(d, e)** Geographical distribution of O$_3$ chemical regimes. **(f)** Proportion of three O$_3$ chemical regimes across urban and nonurban areas in 2019 in Shandong (SD) and individual cities (BZ: Binzhou, ZB: Zibo, LC: Liaocheng, LY: Linyi, JNI: Jining).

in rural areas during summertime. The contribution of NO$_2$ and PM$_{2.5}$ exhibits analogous seasonal variability, promoting O$_3$ formation under low pollution conditions while inhibiting O$_3$ when pollution levels are high (Figs. S15 and 18). The elevated NO$_2$ levels in autumn led to a negative contribution to O$_3$, whereas the facilitating effect of PM$_{2.5}$ was enhanced. This stems from the relatively moderate PM$_{2.5}$ con-

centrations slightly affecting photochemical reaction rates, while the increased NO$_2$ amplified the reactive uptake of NO$_2$ by PM$_{2.5}$, generating more OH radicals that promote O$_3$ formation (Lin et al., 2023; Tan et al., 2022). In winter, PM$_{2.5}$ pollution exceeding 75 µg m^{-3} suppressed O$_3$ formation through scattering and absorbing solar radiation that activates atmospheric chemical processes, which counteracted

the promoting effect of high PM$_{2.5}$ through the conversion of NO$_2$ to HONO.

Figure 8a–c show surface distribution and changes in the relative proportions of SHAP values on three pollutants for inferring O$_3$ photochemical regimes. Moving along an urban-to-rural gradient, reactions dominated by RO$_x$ radical self-reactions are continuously enhanced with increasing NO$_x$ SHAP values, resulting in the majority of rural Shandong being situated in NO$_x$-limited regimes. Furthermore, the overall ozone production regimes in Shandong exhibited a transition toward more NO$_x$-limited from 2019 to 2020, with regions dominated by NO$_x$-limited shifting toward being aerosol-inhibited in the Jiaodong Peninsula. The aerosol-inhibited regime differs from the two classically applied tropospheric O$_3$ policy-control regimes. It is attributed to the predominant heterogeneous HO$_2$ uptake by aqueous aerosols, despite comparatively low PM$_{2.5}$ levels during summertime. The marine environment produces liquid aerosol particles with HO$_2$ uptake coefficients exceeding those of dry aerosols by orders of magnitude (H. Song et al., 2022). Concurrently, lower ambient NO$_x$ levels minimize the promotive effects of aerosols on ozone formation (Tan et al., 2022; Kohno et al., 2022). This result is consistent with the findings of Dyson et al. (Dyson et al., 2023), which concluded that the contribution of HO$_2$ sinks onto aerosols on total HO$_2$ could increase for areas with low NO levels. The attenuated responsiveness of O$_3$ formation to VOCs induced by the uptake of HO$_2$ results in enhanced sensitivity of NO$_x$ at the northwestern boundary region of the Jiaodong Peninsula. Collectively, these processes delineate an aerosol-inhibited ozone production regime in this coastal region, reflecting the sensitivity of O$_3$ photochemistry to the HO$_2$ sink. In several cities, including Binzhou, Zibo, Liaocheng, Linyi, and Jining, a greater proportion of urban areas compared to their nonurban counterparts exhibited a VOC-limited regime in 2019, as indicated by the prevalence of red regions in Fig. 8d. The percentage of urban areas in these cities under a VOC-limited regime ranges from 15 % to 43 %, in stark contrast to nonurban areas where such a regime is typically rare (Fig. 8f). The comparison of O$_3$ sensitivities from 2019 to 2020 shows a regional shift towards increased sensitivity to aerosol and NO$_x$, along with a decreased VOC sensitivity as a result of NO$_x$ reduction (Fig. 8a–c). This shift led to the majority of areas in Shandong being dominated by a NO$_x$-limited regime in 2020, with an expanded aerosol-inhibited regime region in the Jiaodong Peninsula (Fig. 8e). Additionally, the discrepancy in O$_3$ formation sensitivity between urban and nonurban areas was diminished during this period (Fig. 8c). As illustrated in Fig. 9, while the ozone regime transitions towards NO$_x$-limited, there is a marked shift towards greater aerosol sensitivity across nearly 90 % of areas, leading to a 1.6 % increase in aerosol-inhibited grids. Compared to nonurban regions, a higher number of grids in urban areas demonstrate a shift towards NO$_x$ sensitivity. Conversely, urban areas that were predominantly
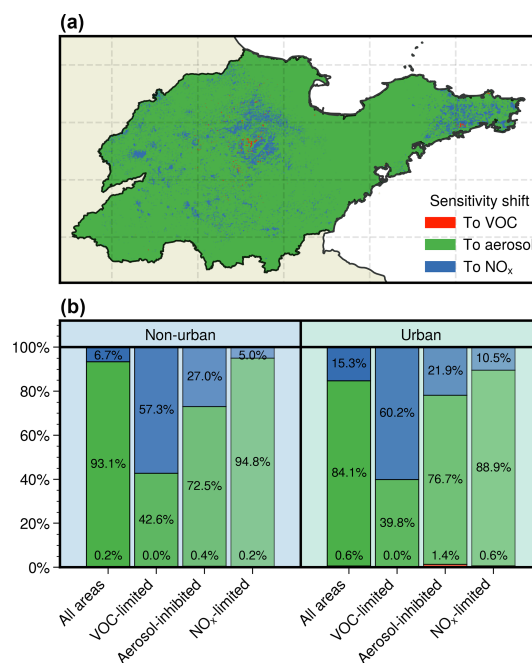
Figure 9. Geographical distribution of changes in ozone sensitivity from 2019 to 2020 in summertime **(a)**. Comparison of ozone sensitivity changes across areas dominated by different chemical regimes in 2019 between urban and nonurban areas **(b)**.

aerosol-inhibited in 2019 showed a lower-sensitivity shift towards NO$_x$.

3.3.2 Impact on urban–nonurban differences

We further explore the reversed O$_3$ differences by separating the individual contributions of climate and anthropogenic changes using an interpretable machine learning model (Fig. 10). The results demonstrate that atmospheric chemical processes and meteorological conditions commonly dominate the discrepancies in O$_3$ levels between urban and nonurban areas. From 2019 to 2020, meteorological shifts remained uniform across urban and nonurban regions, marked by lowered surface pressure, boundary layer height, and shortwave radiation, alongside heightened precipitation. This, coupled with decreased precursor levels, contributed to a decline in O$_3$ pollution. As shown in Figs. 10 and S19, the diminished reduction in boundary layer height and radiation flux across urban areas, compared to nonurban areas in 2020, decelerated the expected decline of O$_3$ concentrations, leading to urban O$_3$ levels exceeding those of nonurban areas. Concurrently, a narrowing difference in temperatures between urban and nonurban areas, despite an overall cooling from 2019 to 2020, favored O$_3$ formation in urban regions during the summertime. Additionally, PM$_{2.5}$ emerged as the principal anthropogenic factor inverting the urban–nonurban O$_3$ disparity over the course of 2019 to 2020. Its contribution to ozone shifted from being lower in urban areas to exceeding
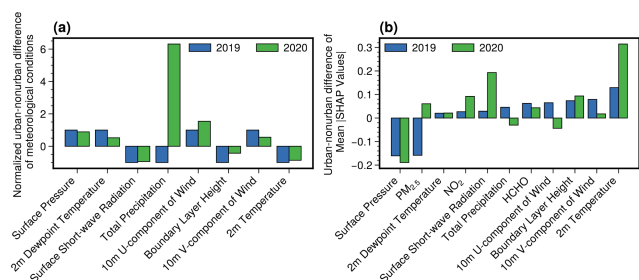
Figure 10. Comparison of urban–nonurban disparities in meteorological conditions **(a)** and mean absolute SHAP values **(b)** between 2019 and 2020 across Shandong, China, during the summertime.

that in nonurban areas, revealing that the decreased reactive uptake of HO$_2$ from aerosols induced by a more substantial reduction in PM$_{2.5}$ in urban areas made the larger contribution to O$_3$ production (Ivatt et al., 2022; Li et al., 2017). Moreover, the response of O$_3$ to the changes in its precursors and PM$_{2.5}$ was determined by the O$_3$ formation regimes. The variations in O$_3$ sensitivity also corroborate the above finding. In rural areas, where there was less of a reduction in PM$_{2.5}$ concentration, the sensitivity increasingly favored aerosol suppression across more than 93 % of the assessed grids (Fig. 9). This enhanced suppression effect of aerosols in rural areas leads to a more significant O$_3$ reduction compared to urban locales. The reduction of NO$_x$ in nonurban areas demonstrated a more effective reduction in O$_3$ levels, which predominantly shifted towards a NO$_x$-limited regime in 2020. Although urban areas also showed a shift towards being a NO$_x$-limited regime, they exhibited relatively higher sensitivity to VOCs (Fig. 8). The urban areas, characterized by elevated NO$_x$ emissions, exhibited a higher sensitivity to VOCs, and the fraction of aerosol-inhibited areas increased from 2019 to 2020, resulting in the control benefits of urban O$_3$ pollution in 2020 being partially offset by the nonlinear response of O$_3$ to a greater reduction in NO$_2$ and PM$_{2.5}$, as well as a smaller decrease in HCHO relative to nonurban areas. Consequently, O$_3$ exhibits a lower reduction in urban areas as a result of the aforementioned changes.

4 Conclusions

The purpose of the current study was to diagnose the nonlinearity of O$_3$–NO$_x$–VOC–aerosol chemistry using an interpretable ML model based on spatially resolved multipollutant estimations for determining the causes of changing differences in O$_3$ levels between urban and nonurban areas. Our study represents the first attempt to develop an advanced DL model that reconstructs the concentrations of multiple pollutants and subsequently infers the aerosol-inhibited regime from observations. This innovative approach provides further support for investigating the impact of precursor

emissions and aerosol on the urban–nonurban differences in O$_3$ levels.

Given the nonlinearity of ozone formation and its increasing regional differences, precise estimations of ground-level O$_3$, NO$_2$, HCHO, and PM$_{2.5}$ are crucial for deducing the chemical regimes governing ozone pollution and its urban–nonurban disparities. The evaluation of the model's performance indicates that it can be readily extended to any other domain thanks to its unified architecture. Anyone can easily utilize the model to estimate ground-level pollutants, intelligently considering spatial–temporal neighborhood information based on their customized input data. The model further improved spatial resolution to sub-kilometer levels using TROPOMI and MODIS retrievals via spatiotemporal autocorrelation downscaling of AiT. The "black box" nature of AiT can be made more physically interpretable by SHAP, enabling the evaluation of the significance of each input variable (Fig. S20). The season trends show the highest contribution, followed by emission proxies and meteorological conditions. Meanwhile, the results between AiT trained with all data and that trained exclusively with CNEMC data across various spatiotemporal scales underscore the promising prospect for improving the model's generalization ability with more ground-level monitoring data and the growing space of methods.

We conclude that with the effective reduction of PM$_{2.5}$ pollution, the sensitivity of O$_3$ to VOCs will increase, necessitating further intensification of VOC emission regulation by government agencies. Three distinct chemical regimes were assessed by tracking NO$_x$, VOCs, and aerosols with surface NO$_2$, HCHO, and PM$_{2.5}$. In the Jiaodong Peninsula of Shandong province, coastal areas with relatively few primary pollutants are widely found to be under an aerosol suppression regime, illustrating that ozone regime inference based on machine learning can serve as an alternative to determining the aerosol suppression regime through the rate of radical termination in atmospheric chemical models. The O$_3$ regime in other areas of Shandong generally transitioned from the NO$_x$-sensitive regime in nonurban to a more VOC-sensitive regime in urban areas. We estimate that substantial reductions in anthropogenic emissions of PM$_{2.5}$ and NO$_2$ are the main drivers of the reversal of the traditional discrepancy in O$_3$ levels between urban and nonurban areas. In essence, due to the lower efforts in reducing PM$_{2.5}$ in nonurban settings, the aerosol-mediated suppression of ozone became more pronounced, resulting in lower ozone levels in rural areas relative to urban centers. This shift underlines the intricate balance between emission reduction and ozone formation mechanisms, suggesting that nuanced understanding and targeted interventions are necessary to manage and mitigate the health and environmental impacts of such disparities. To preclude exacerbated O$_3$ pollution resulting from the shift of many regions from VOC-limited to NO$_x$-limited regimes and the decline in heterogeneous HO$_2$ uptake induced by PM$_{2.5}$ reduction in urban areas, emission policies aimed at decreasing

NO$_x$ to reduce O$_3$ levels will only be effective with stringent VOC emission abatement when PM$_{2.5}$ is concurrently decreased. The integration of high-resolution pollutant estimations with an interpretable machine learning model offers a promising avenue for advancing our understanding of ozone pollution dynamics and developing effective air quality management strategies.

Although our study endeavors to establish O$_3$ formation regimes involving NO$_x$, VOCs, and aerosols, and the method identifies an aerosol-inhibited regime from a statistical perspective, it is subject to certain uncertainties due to the relatively poor data quality of HCHO and the unsegregated multiple impacts of aerosols, such as N$_2$O$_5$ uptake, NO$_2$ uptake, HO$_2$ uptake, and light extinction (Tan et al., 2022). We have made efforts to integrate all required surface pollutant concentrations into a unified model, while the absence of ground-level HCHO monitoring data compelled us to tap into an alternative methodology. The retrieval error of surface HCHO and the system error between its retrieval approach and the AiT model degrade the ability of ML to identify the O$_3$ sensitivity. Meanwhile, the notion of ozone regimes is only appreciated in photochemically active environments where the RO$_x$–HO$_x$ cycle is active (Souri et al., 2023). The definition of NO$_x$-limited or VOC-limited regimes is meaningless in nighttime chemistry, where NO–O$_3$–NO$_2$ partitioning is the primary driver. The surface daytime pollutant estimations with finer resolutions in space and time based on a unified modeling framework will offer an unprecedented view to characterize the near-surface O$_3$ formation regimes. Notwithstanding the relatively limited duration of the study, this work offers valuable insights into the current state and causes of urban–nonurban disparities in O$_3$ pollution. Future efforts should conduct a more detailed long-term evaluation of urban–nonurban disparities in global O$_3$ levels and the impact of formation mechanisms to further our understanding of air pollution and its mitigation.

Author contributions. CT: methodology, software, validation, formal analysis, investigation, data curation, writing (original draft), visualization. YP: conceptualization, writing (review and editing). QZ: writing (review and editing), project administration, funding acquisition. YZ: methodology, writing (review and editing). BG: software, writing (review and editing). QW: supervision, writing (review and editing). WW: supervision, writing (review and editing).

References

Action Plan on Air Pollution Prevention and Control (in Chinese): http://www.gov.cn/zwgk/2013-09/12/content_2486773.htm (last access: 1 February 2023), 2023.

Bertasius, G., Wang, H., and Torresani, L.: Is Space-Time Attention All You Need for Video Understanding?, arXiv [preprint], https://doi.org/10.48550/arXiv.2102.05095, 9 June 2021.

Chen, T. and Guestrin, C.: XGBoost: A Scalable Tree Boosting System, in: Proceedings of the 22nd ACM SIGKDD International Conference on Knowledge Discovery and Data Mining, KDD'16: The 22nd ACM SIGKDD International Conference on Knowledge Discovery and Data Mining, San Francisco California USA, 785–794, https://doi.org/10/gdp84q, 2016.

Chu, W., Li, H., Ji, Y., Zhang, X., Xue, L., Gao, J., and An, C.: Research on ozone formation sensitivity based on observational methods: Development history, methodology, and application and prospects in China, J. Environ. Sci., 138, 543–560, https://doi.org/10/gr4qzk, 2023.

Cooper, M. J., Martin, R. V., Hammer, M. S., Levelt, P. F., Veefkind, P., Lamsal, L. N., Krotkov, N. A., Brook, J. R., and McLinden, C. A.: Global fine-scale changes in ambient NO$_2$ during COVID-19 lockdowns, Nature, 601, 380–387, https://doi.org/10.1038/s41586-021-04229-0, 2022.

Copernicus Sentinel-5P (processed by ESA): TROPOMI Level 2 Ozone Total Column products (Version 02), European Space Agency [data set], https://doi.org/10.5270/S5P-ft13p57, 2020.

Di, Q., Kloog, I., Koutrakis, P., Lyapustin, A., Wang, Y., and Schwartz, J.: Assessing PM$_{2.5}$ Exposures with High Spatiotemporal Resolution across the Continental United States, Environ. Sci. Technol., 50, 4712–4721, https://doi.org/10.1021/acs.est.5b06121, 2016.

Dias, D. and Tchepel, O.: Spatial and Temporal Dynamics in Air Pollution Exposure Assessment, IJERPH, 15, 558, https://doi.org/10.3390/ijerph15030558, 2018.

Didan, K.: MODIS/Terra Vegetation Indices 16-Day L3 Global 250 m SIN Grid V061, NASA EOSDIS Land Processes Distributed Active Archive Center [data set], https://doi.org/10.5067/MODIS/MOD13Q1.061, 2021.

Dosovitskiy, A., Beyer, L., Kolesnikov, A., Weissenborn, D., Zhai, X., Unterthiner, T., Dehghani, M., Minderer, M., Heigold, G., Gelly, S., Uszkoreit, J., and Houlsby, N.: An Image is Worth 16x16 Words: Transformers for Image Recognition at Scale, arXiv [preprint], https://doi.org/10.48550/arXiv.2010.11929, 3 June 2021.

Dyson, J. E., Whalley, L. K., Slater, E. J., Woodward-Massey, R., Ye, C., Lee, J. D., Squires, F., Hopkins, J. R., Dunmore, R. E., Shaw, M., Hamilton, J. F., Lewis, A. C., Worrall, S. D., Bacak, A., Mehra, A., Bannan, T. J., Coe, H., Percival, C. J., Ouyang, B., Hewitt, C. N., Jones, R. L., Crilley, L. R., Kramer, L. J., Acton, W. J. F., Bloss, W. J., Saksakulkrai, S., Xu, J., Shi, Z., Harrison, R. M., Kotthaus, S., Grimmond, S., Sun, Y., Xu, W., Yue, S., Wei, L., Fu, P., Wang, X., Arnold, S. R., and Heard, D. E.: Impact of HO$_2$ aerosol uptake on radical levels and O$_3$ production during summertime in Beijing, Atmos. Chem. Phys., 23, 5679–5697, https://doi.org/10.5194/acp-23-5679-2023, 2023.

Geng, G., Xiao, Q., Liu, S., Liu, X., Cheng, J., Zheng, Y., Xue, T., Tong, D., Zheng, B., Peng, Y., Huang, X., He, K., and Zhang, Q.: Tracking Air Pollution in China: Near Real-Time PM$_{2.5}$ Retrievals from Multisource Data Fusion, Environ. Sci. Technol., 55, 12106–12115, https://doi.org/10.1021/acs.est.1c01863, 2021.

Global Modeling and Assimilation Office (GMAO): MERRA-2 inst3_2d_gas_Nx: 2d, 3-Hourly, Instantaneous, Single-Level, Assimilation, Aerosol Optical Depth Analysis V5.12.4, Goddard Earth Sciences Data and Information Services Center (GES DISC) [data set], Greenbelt, MD, USA, https://doi.org/10.5067/HNGA0EWW0R09, 2015.

Han, H., Zhang, L., Liu, Z., Yue, X., Shu, L., Wang, X., and Zhang, Y.: Narrowing Differences in Urban and Nonurban Surface Ozone in the Northern Hemisphere Over 1990–2020, Environ. Sci. Technol. Lett., 10, 410–417, https://doi.org/10/gsd5gk, 2023.

Han, X. and Naeher, L. P.: A review of traffic-related air pollution exposure assessment studies in the developing world, Environ. Int., 32, 106–120, https://doi.org/10.1016/j.envint.2005.05.020, 2006.

Hersbach, H., Bell, B., Berrisford, G., Horányi, A., Muñoz Sabater, J., Nicolas, J., Peubey, C., Rozum, I., Schepers, D., Simmons, A., Soci, C., Dee, D., and Thépaut, J.-N.: ERA5 hourly data on single levels from 1959 to present, Copernicus Climate Change Service (C3S) Climate Data Store (CDS) [data set], https://doi.org/10.24381/cds.adbb2d47, 2023.

Huang, C., Hu, J., Xue, T., Xu, H., and Wang, M.: High-Resolution Spatiotemporal Modeling for Ambient PM$_{2.5}$ Exposure Assessment in China from 2013 to 2019, Environ. Sci. Technol., 55, 2152–2162, https://doi.org/10.1021/acs.est.0c05815, 2021.

Inness, A., Ades, M., Agustí-Panareda, A., Barré, J., Benedictow, A., Blechschmidt, A.-M., Dominguez, J. J., Engelen, R., Eskes, H., Flemming, J., Huijnen, V., Jones, L., Kipling, Z., Massart, S., Parrington, M., Peuch, V.-H., Razinger, M., Remy, S., Schulz, M., and Suttie, M.: The CAMS reanalysis of atmospheric composition, Atmos. Chem. Phys., 19, 3515–3556, https://doi.org/10.5194/acp-19-3515-2019, 2019.

Ivatt, P. D., Evans, M. J., and Lewis, A. C.: Suppression of surface ozone by an aerosol-inhibited photochemical ozone regime, Nat. Geosci., 15, 536–540, https://doi.org/10.1038/s41561-022-00972-9, 2022.

Jerrett, M., Arain, A., Kanaroglou, P., Beckerman, B., Potoglou, D., Sahsuvaroglu, T., Morrison, J., and Giovis, C.: A review and evaluation of intraurban air pollution exposure models, J. Expo. Sci. Env. Epid., 15, 185–204, https://doi.org/10.1038/sj.jea.7500388, 2005.

Jin, X., Fiore, A. M., Murray, L. T., Valin, L. C., Lamsal, L. N., Duncan, B., Folkert Boersma, K., De Smedt, I., Abad, G. G., Chance, K., and Tonnesen, G. S.: Evaluating a Space-Based Indicator of Surface Ozone-NO$_x$-VOC Sensitivity Over Midlatitude Source Regions and Application to Decadal Trends: Space-Based Indicator of O$_3$ Sensitivity, J. Geophys. Res.-Atmos., 122, 10439–10461, https://doi.org/10.1002/2017JD026720, 2017.

Jin, X., Fiore, A., Boersma, K. F., Smedt, I. D., and Valin, L.: Inferring Changes in Summertime Surface Ozone-NO$_x$-VOC Chemistry over U.S. Urban Areas from Two Decades of Satellite and Ground-Based Observations, Environ. Sci. Technol., 54, 6518–6529, https://doi.org/10.1021/acs.est.9b07785, 2020.

Jin, X., Fiore, A. M., and Cohen, R. C.: Space-Based Observations of Ozone Precursors within California Wildfire Plumes and the Impacts on Ozone-NO$_x$-VOC Chemistry, Environ. Sci. Technol., 57, 14648–14660, https://doi.org/10.1021/acs.est.3c04411, 2023.

Jun, C., Ban, Y., and Li, S.: China: Open access to Earth land-cover map, Nature, 514, 434–434, https://doi.org/10.1038/514434c, 2014.

Jung, J., Choi, Y., Souri, A. H., Mousavinezhad, S., Sayeed, A., and Lee, K.: The Impact of Springtime-Transported Air Pollutants on Local Air Quality With Satellite-Constrained NO$_x$ Emission Adjustments Over East Asia, J. Geophys. Res.-Atmos., 127, e2021JD035251, https://doi.org/10.1029/2021JD035251, 2022.

Ke, G., Meng, Q., Finley, T., Wang, T., Chen, W., Ma, W., Ye, Q., and Liu, T.-Y.: LightGBM: A Highly Efficient Gradient Boosting Decision Tree, in: Proceedings of the 31st International Conference on Neural Information Processing Systems, Red Hook, NY, USA, event-place: Long Beach, California, USA, 3149–3157, 2017.

Kohno, N., Zhou, J., Li, J., Takemura, M., Ono, N., Sadanaga, Y., Nakashima, Y., Sato, K., Kato, S., Sakamoto, Y., and Kajii, Y.: Impacts of missing OH reactivity and aerosol uptake of HO$_2$ radicals on tropospheric O$_3$ production during the AQUAS-Kyoto summer campaign in 2018, Atmos. Environ., 281, 119130, https://doi.org/10/gshfc4, 2022.

Lamsal, L. N., Krotkov, N. A., Marchenko, S. V., Joiner, J., Oman, L., Vasilkov, A., Fisher, B., Qin, W., Yang, E.-S., Fas-

nacht, Z., Choi, S., Leonard, P., and Haffner, D.: TROPOMI/S5P NO$_2$ Tropospheric, Stratospheric and Total Columns MINDS 1-Orbit L2 Swath 5.5 km × 3.5 km, Goddard Earth Sciences Data and Information Services Center (GES DISC) [data set], https://doi.org/10.5067/MEASURES/MINDS/DATA203, 2022.

Lee, H. J., Kuwayama, T., and FitzGibbon, M.: Trends of ambient O$_3$ levels associated with O$_3$ precursor gases and meteorology in California: Synergies from ground and satellite observations, Remote Sens. Environ., 284, 113358, https://doi.org/10.1016/j.rse.2022.113358, 2023.

Li, C., Zhu, Q., Jin, X., and Cohen, R. C.: Elucidating Contributions of Anthropogenic Volatile Organic Compounds and Particulate Matter to Ozone Trends over China, Environ. Sci. Technol., 56, 12906–12916, https://doi.org/10.1021/acs.est.2c03315, 2022.

Li, D., Wang, S., Xue, R., Zhu, J., Zhang, S., Sun, Z., and Zhou, B.: OMI-observed HCHO in Shanghai, China, during 2010–2019 and ozone sensitivity inferred by an improved HCHO/NO$_2$ ratio, Atmos. Chem. Phys., 21, 15447–15460, https://doi.org/10.5194/acp-21-15447-2021, 2021.

Li, K., Jacob, D. J., Liao, H., Zhu, J., Shah, V., Shen, L., Bates, K. H., Zhang, Q., and Zhai, S.: A two-pollutant strategy for improving ozone and particulate air quality in China, Nat. Geosci., 12, 906–910, https://doi.org/10.1038/s41561-019-0464-x, 2019.

Li, K., Wang, Y., Peng, G., Song, G., Liu, Y., Li, H., and Qiao, Y.: UniFormer: Unified Transformer for Efficient Spatial-Temporal Representation Learning, International Conference on Learning Representations, Virtual, 25–29 April 2022, 2021.

Li, L. and Wu, J.: Spatiotemporal estimation of satellite-borne and ground-level NO$_2$ using full residual deep networks, Remote Sens. Environ., 254, 112257, https://doi.org/10.1016/j.rse.2020.112257, 2021.

Li, M., Wang, T., Xie, M., Zhuang, B., Li, S., Han, Y., and Chen, P.: Impacts of aerosol-radiation feedback on local air quality during a severe haze episode in Nanjing megacity, eastern China, Tellus B, 69, 1339548, https://doi.org/10/gsfjz3, 2017.

Li, M., Yang, Q., Yuan, Q., and Zhu, L.: Estimation of high spatial resolution ground-level ozone concentrations based on Landsat 8 TIR bands with deep forest model, Chemosphere, 301, 134817, https://doi.org/10.1016/j.chemosphere.2022.134817, 2022.

Lin, C., Huang, R.-J., Zhong, H., Duan, J., Wang, Z., Huang, W., and Xu, W.: Elucidating ozone and PM$_{2.5}$ pollution in the Fenwei Plain reveals the co-benefits of controlling precursor gas emissions in winter haze, Atmos. Chem. Phys., 23, 3595–3607, https://doi.org/10.5194/acp-23-3595-2023, 2023.

Liu, M., Huang, Y., Ma, Z., Jin, Z., Liu, X., Wang, H., Liu, Y., Wang, J., Jantunen, M., Bi, J., and Kinney, P. L.: Spatial and temporal trends in the mortality burden of air pollution in China: 2004–2012, Environ. Int., 98, 75–81, https://doi.org/10.1016/j.envint.2016.10.003, 2017.

Liu, X., Shi, X., Lei, Y., and Xue, W.: Path of coordinated control of PM$_{2.5}$ and ozone in China, Chin. Sci. Bull., 67, 2089–2099, https://doi.org/10.1360/TB-2021-0832, 2022.

Lu, D., Mao, W., Zheng, L., Xiao, W., Zhang, L., and Wei, J.: Ambient PM$_{2.5}$ Estimates and Variations during COVID-19 Pandemic in the Yangtze River Delta Using Machine Learning and Big Data, Remote Sens., 13, 1423, https://doi.org/10.3390/rs13081423, 2021.

Lu, X., Hong, J., Zhang, L., Cooper, O. R., Schultz, M. G., Xu, X., Wang, T., Gao, M., Zhao, Y., and Zhang, Y.: Severe Surface Ozone Pollution in China: A Global Perspective, Environ. Sci. Technol. Lett., 5, 487–494, https://doi.org/10.1021/acs.estlett.8b00366, 2018.

Lundberg, S. M. and Lee, S.-I.: A Unified Approach to Interpreting Model Predictions, in: Proceedings of the 31st International Conference on Neural Information Processing Systems, Long Beach, California, USA, 4–9 December 2017, Red Hook, NY, USA, 4768–4777, 2017.

Lyapustin, A. and Wang, Y.: MODIS/Terra+Aqua Land Aerosol Optical Depth Daily L2G Global 1 km SIN Grid V061, NASA EOSDIS Land Processes DAAC [data set], https://doi.org/10.5067/MODIS/MCD19A2.061, 2022.

Miller, D. F., Alkezweeny, A. J., Hales, J. M., and Lee, R. N.: Ozone Formation Related to Power Plant Emissions, Science, 202, 1186–1188, https://doi.org/10/b5kgjr, 1978.

Mitchell, R., Frank, E., and Holmes, G.: GPUTreeShap: massively parallel exact calculation of SHAP scores for tree ensembles, PeerJ Comput. Sci., 8, e880, https://doi.org/10.7717/peerj-cs.880, 2020.

Myers, S. L.: The Worst Dust Storm in a Decade Shrouds Beijing and Northern China, The New York Times, https://www.nytimes.com/2021/03/15/world/asia/china-sandstorm.html (last access: 12 March 2023), 15 March 2021.

Pusede, S. E., Steiner, A. L., and Cohen, R. C.: Temperature and Recent Trends in the Chemistry of Continental Surface Ozone, Chem. Rev., 115, 3898–3918, https://doi.org/10.1021/cr5006815, 2015.

Ren, J., Guo, F., and Xie, S.: Diagnosing ozone–NO$_x$–VOC sensitivity and revealing causes of ozone increases in China based on 2013–2021 satellite retrievals, Atmos. Chem. Phys., 22, 15035–15047, https://doi.org/10.5194/acp-22-15035-2022, 2022.

Ren, X., Mi, Z., Cai, T., Nolte, C. G., and Georgopoulos, P. G.: Flexible Bayesian Ensemble Machine Learning Framework for Predicting Local Ozone Concentrations, Environ. Sci. Technol., 56, 3871–3883, https://doi.org/10.1021/acs.est.1c04076, 2022.

Requia, W. J., Di, Q., Silvern, R., Kelly, J. T., Koutrakis, P., Mickley, L. J., Sulprizio, M. P., Amini, H., Shi, L., and Schwartz, J.: An Ensemble Learning Approach for Estimating High Spatiotemporal Resolution of Ground-Level Ozone in the Contiguous United States, Environ. Sci. Technol., 54, 11037–11047, https://doi.org/10.1021/acs.est.0c01791, 2020.

Román, M. O., Wang, Z., Sun, Q., Kalb, V., Miller, S. D., Molthan, A., Schultz, L., Bell, J., Stokes, E. C., Pandey, B., Seto, K. C., Hall, D., Oda, T., Wolfe, R. E., Lin, G., Golpayegani, N., Devadiga, S., Davidson, C., Sarkar, S., Praderas, C., Schmaltz, J., Boller, R., Stevens, J., Ramos González, O. M., Padilla, E., Alonso, J., Detrés, Y., Armstrong, R., Miranda, I., Conte, Y., Marrero, N., MacManus, K., Esch, T., and Masuoka, E. J.: NASA's Black Marble nighttime lights product suite, Remote Sens. Environ., 210, 113–143, https://doi.org/10/ghqpjh, 2018.

Shapley, L. S.: A value for n-person games, in: The Shapley Value: Essays in Honor of Lloyd S. Shapley, edited by: Roth, A. E., Cambridge University Press, Cambridge, 31–40, https://doi.org/10.1017/CBO9780511528446.003, 1988.

Shrikumar, A., Greenside, P., and Kundaje, A.: Learning Important Features Through Propagating Activation Differences, in: International conference on machine learning, Sydney NSW Australia, 6–11 August 2017, 3145–3153, 2017.

Sicard, P., Serra, R., and Rossello, P.: Spatiotemporal trends in ground-level ozone concentrations and metrics in France over the time period 1999–2012, Environ. Res., 149, 122–144, https://doi.org/10.1016/j.envres.2016.05.014, 2016.

Sicard, P., De Marco, A., Agathokleous, E., Feng, Z., Xu, X., Paoletti, E., Rodriguez, J. J. D., and Calatayud, V.: Amplified ozone pollution in cities during the COVID-19 lockdown, Sci. Total Environ., 735, 139542, https://doi.org/10/gg5w8h, 2020.

Sillman, S.: The use of NO$_y$, H$_2$O$_2$, and HNO$_3$ as indicators for ozone-NO$_x$-hydrocarbon sensitivity in urban locations, J. Geophys. Res., 100, 14175, https://doi.org/10.1029/94JD02953, 1995.

Song, H., Lu, K., Dong, H., Tan, Z., Chen, S., Zeng, L., and Zhang, Y.: Reduced Aerosol Uptake of Hydroperoxyl Radical May Increase the Sensitivity of Ozone Production to Volatile Organic Compounds, Environ. Sci. Technol. Lett., 9, 22–29, https://doi.org/10/gnqqb9, 2022.

Song, K., Liu, R., Wang, Y., Liu, T., Wei, L., Wu, Y., Zheng, J., Wang, B., and Liu, S. C.: Observation-based analysis of ozone production sensitivity for two persistent ozone episodes in Guangdong, China, Atmos. Chem. Phys., 22, 8403–8416, https://doi.org/10.5194/acp-22-8403-2022, 2022.

Souri, A. H., Johnson, M. S., Wolfe, G. M., Crawford, J. H., Fried, A., Wisthaler, A., Brune, W. H., Blake, D. R., Weinheimer, A. J., Verhoelst, T., Compernolle, S., Pinardi, G., Vigouroux, C., Langerock, B., Choi, S., Lamsal, L., Zhu, L., Sun, S., Cohen, R. C., Min, K.-E., Cho, C., Philip, S., Liu, X., and Chance, K.: Characterization of errors in satellite-based HCHO/NO$_2$ tropospheric column ratios with respect to chemistry, column-to-PBL translation, spatial representation, and retrieval uncertainties, Atmos. Chem. Phys., 23, 1963–1986, https://doi.org/10.5194/acp-23-1963-2023, 2023.

Su, W., Hu, Q., Chen, Y., Lin, J., Zhang, C., and Liu, C.: Inferring global surface HCHO concentrations from multisource hyperspectral satellites and their application to HCHO-related global cancer burden estimation, Environ. Int., 170, 107600, https://doi.org/10.1016/j.envint.2022.107600, 2022.

Sun, H., Shin, Y. M., Xia, M., Ke, S., Wan, M., Yuan, L., Guo, Y., and Archibald, A. T.: Spatial Resolved Surface Ozone with Urban and Rural Differentiation during 1990–2019: A Space – Time Bayesian Neural Network Downscaler, Environ. Sci. Technol., 56, 7337–7349, https://doi.org/10.1021/acs.est.1c04797, 2022.

Tan, Z., Lu, K., Ma, X., Chen, S., He, L., Huang, X., Li, X., Lin, X., Tang, M., Yu, D., Wahner, A., and Zhang, Y.: Multiple Impacts of Aerosols on O$_3$ Production Are Largely Compensated: A Case Study Shenzhen, China, Environ. Sci. Technol., 56, 17569–17580, https://doi.org/10/gsgp79, 2022.

Tang, L., Xue, X., Qu, J., Mi, Z., Bo, X., Chang, X., Wang, S., Li, S., Cui, W., and Dong, G.: Air pollution emissions from Chinese power plants based on the continuous emission monitoring systems network, Sci. Data, 7, 325, https://doi.org/10/ghfqqf, 2020.

Tao, C.: Surface Ozone, NO$_2$, and PM$_{2.5}$ Concentrations Estimated by the Deep Learning model (Air Transformer) based on Satellite data, Zenodo [data set], https://doi.org/10.5281/zenodo.10071408, 2023.

Tao, C.: myles-tcl/Air-Transformer: V1.0.0 (publish), Zenodo [code], https://doi.org/10.5281/zenodo.10889597, 2024.

Thongthammachart, T., Araki, S., Shimadera, H., Matsuo, T., and Kondo, A.: Incorporating Light Gradient Boosting Machine to land use regression model for estimating NO$_2$ and PM$_{2.5}$ levels in Kansai region, Japan, Environ. Modell. Softw., 155, 105447, https://doi.org/10.1016/j.envsoft.2022.105447, 2022.

van Donkelaar, A., Martin, R. V., Spurr, R. J. D., and Burnett, R. T.: High-Resolution Satellite-Derived PM$_{2.5}$ from Optimal Estimation and Geographically Weighted Regression over North America, Environ. Sci. Technol., 49, 10482–10491, https://doi.org/10.1021/acs.est.5b02076, 2015.

Wei, J., Li, Z., Li, K., Dickerson, R. R., Pinker, R. T., Wang, J., Liu, X., Sun, L., Xue, W., and Cribb, M.: Full-coverage mapping and spatiotemporal variations of ground-level ozone (O$_3$) pollution from 2013 to 2020 across China, Remote Sens. Environ., 270, 112775, https://doi.org/10.1016/j.rse.2021.112775, 2022a.

Wei, J., Liu, S., Li, Z., Liu, C., Qin, K., Liu, X., Pinker, R. T., Dickerson, R. R., Lin, J., Boersma, K. F., Sun, L., Li, R., Xue, W., Cui, Y., Zhang, C., and Wang, J.: Ground-Level NO$_2$ Surveillance from Space Across China for High Resolution Using Interpretable Spatiotemporally Weighted Artificial Intelligence, Environ. Sci. Technol., 56, 9988–9998, https://doi.org/10.1021/acs.est.2c03834, 2022b.

Wei, W., Wang, X., Wang, X., Li, R., Zhou, C., and Cheng, S.: Attenuated sensitivity of ozone to precursors in Beijing–Tianjin–Hebei region with the continuous NOx reduction within 2014–2018, Sci. Total Environ., 813, 152589, https://doi.org/10/gq7ngn, 2022.

WorldPop: Global High Resolution Population Denominators Project – Funded by The Bill and Melinda Gates Foundation (OPP1134076) [data set], https://doi.org/10.5258/SOTON/WP00675, 2018.

Xiao, Q., Chang, H. H., Geng, G., and Liu, Y.: An Ensemble Machine-Learning Model To Predict Historical PM$_{2.5}$ Concentrations in China from Satellite Data, Environ. Sci. Technol., 52, 13260–13269, https://doi.org/10.1021/acs.est.8b02917, 2018.

Yue, X., Unger, N., Harper, K., Xia, X., Liao, H., Zhu, T., Xiao, J., Feng, Z., and Li, J.: Ozone and haze pollution weakens net primary productivity in China, Atmos. Chem. Phys., 17, 6073–6089, https://doi.org/10.5194/acp-17-6073-2017, 2017.

Zhang, J., Wang, J., Sun, Y., Li, J., Ninneman, M., Ye, J., Li, K., Crandall, B., Mao, J., Xu, W., Schwab, M. J., Li, W., Ge, X., Chen, M., Ying, Q., Zhang, Q., and Schwab, J. J.: Insights from ozone and particulate matter pollution control in New York City applied to Beijing, Clim. Atmos. Sci., 5, 85, https://doi.org/10.1038/s41612-022-00309-8, 2022.

Zhang, R., Lei, W., Tie, X., and Hess, P.: Industrial emissions cause extreme urban ozone diurnal variability, P. Natl. Acad. Sci. USA, 101, 6346–6350, https://doi.org/10.1073/pnas.0401484101, 2004.

Zhao, M., Cheng, C., Zhou, Y., Li, X., Shen, S., and Song, C.: A global dataset of annual urban extents (1992–2020) from harmonized nighttime lights, Earth Syst. Sci. Data, 14, 517–534, https://doi.org/10.5194/essd-14-517-2022, 2022.

Zheng, B., Tong, D., Li, M., Liu, F., Hong, C., Geng, G., Li, H., Li, X., Peng, L., Qi, J., Yan, L., Zhang, Y., Zhao, H., Zheng, Y., He, K., and Zhang, Q.: Trends in China's anthropogenic emissions since 2010 as the consequence of clean air actions, Atmos. Chem. Phys., 18, 14095–14111, https://doi.org/10.5194/acp-18-14095-2018, 2018.